České vysoké učení technické v Praze
Fakulta jaderná a fyzikálně inženýrská

Katedra fyziky

Obor: Jaderná a částicová fyzika

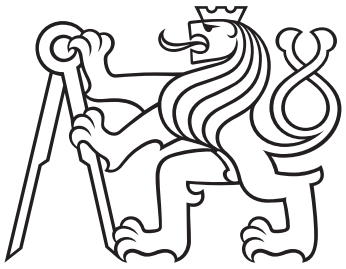

Electrons from open heavy-flavor hadron decays in heavy-ion collisions at STAR

VÝZKUMNÝ ÚKOL

Vypracoval:	Carolina Sergi Lopes
Vedoucí práce:	Dr. Barbara Antonina Trzeciak, Ph.D.
Konzultant:	Mgr. Ing. Leszek Kosarzewski, Ph.D.
Rok:	2021

CZECH TECHNICAL UNIVERSITY IN PRAGUE
FACULTY OF NUCLEAR SCIENCES
AND PHYSICAL ENGINEERING
Břehová 7, 115 19 Praha 1

Department: Physics **Academic year:** 2020/2021

RESEARCH TASK

Student: Carolina Sergi Lopes

Study program: Nuclear and Particle Physics

Advisor: Dr. Barbara Antonina Trzeciak, Ph.D.

Consultant - Mgr. Ing. Leszek Kosarzewski, Ph.D.

Title of the task (english/czech):
Electrons from open heavy-flavour hadron decays in heavy-ion collisions at STAR/
Elektrony z rozpadů těžkých hadronů otevřených vůní v jádro-jaderných srážkách na experimentu STAR

Instructions:

1. Overview of results on open heavy-flavour hadron production in proton-proton and heavy-ion collisions.
2. STAR experiment.
3. Identification of inclusive and photonic electrons in the STAR experiment.
4. Reconstruction of heavy-flavour electrons and corrections.
5. Discussion and conclusions.

Part of the instructions is the requirement that the research task will be presented at the webpage of the department of physics.

Literature:

1. H. Satz: Extreme States of Matter in Strong Interaction Physics. Lecture Notes in Physics 945, Springer, 2018
2. X.Dong, Y-J. Lee and R. Rapp: Open Heavy-Flavor Production in Heavy-Ion Collisions. Ann. ReV. Nucl. Part. Sci. 69, 4170445 (2019)
3. X. Dong and V. Greco: Heavy quark production and properties of Quark–Gluon Plasma. Progress in Particle and Nuclear Physics 104 (2019) 97–141
4. L. Adamczyk, et. al: Elliptic flow of electrons from heavy-flavor hadron decays in Au+Au collisions at 200, 62.4 and 39 GeV, Phys. Rev. C 95, 034907 (2017)
5. M. Mustafa: Experimental study of electrons from heavy flavor hadrons decays in Au+Au collisions at 200, 62.4 and 39 GeV in the STAR experiment at RHIC, Ph.D. Thesis, Purdue University, 2013

Date of instructions: 23. 10. 2020 .....

Due date of task: 30. 06. 2021 ***chair of Department of physics***

Čestné prohlášení

Prohlašuji, že jsem svůj Výzkumný úkol vypracoval samostatně a uvedl jsem všechnu použitou literaturu.

Nemám závažný důvod proti použití tohoto školního díla ve smyslu §60 Zákona č. 121/2000 Sb., o právu autorském, o právech souvisejících s právem autorským a o změně některých zákonů (autorský zákon).

V Praze dne 13. září 2021 Carolina Sergi Lopes

Abstract

Here, we report on the steps towards the measurement of the production yield of heavy-flavor electrons (HFE) in Au+Au collisions ($0 - 60\%$ centrality) at $\sqrt{s_{NN}} = 54$ GeV at the STAR Experiment at RHIC. HFE are mainly produced as a result of the semi-leptonic decays of heavy quarks (charm or beauty), which are created during hard processes very early in the collisions. Given this characteristic, they constitute important probes of the Quark-Gluon Plasma properties.

The current main purpose of this study consists in including recent available information from the Barrel Electromagnetic Calorimeter (BEMC) subdetector to improve the electron identification in the referred dataset. According to the parameters obtained from the purity studies and from the analysis of hot BEMC towers, the results can be applied in further studies of the STAR Collaboration. Another priority of this study is the estimation of the purity of the inclusive electron sample, used to calculate the yield of non-photonic electrons.

Future goals of this analysis include the attainment of the non-photonic electron yield, with a possible distinction of HFE from within this sample. Non-photonic electrons are identified within the inclusive electrons by means of statistical methods. The obtained result comprises HFE and electrons from hadron decays (heavy quarkonia, vector mesons and Drell-Yan processes), the first representing the most significant contribution.

After obtaining the heavy-flavor electron yield, the analysis of the energy loss of heavy-flavor electrons in the medium via the calculation of the nuclear modification factors R_{AA} and R_{CP} becomes possible.

Contents

List of Figures

List of Tables

Chapter 1

Introduction

The main purpose of ultrarelativistic heavy-ion collisions studied at experiments such as STAR (RHIC) and ALICE (LHC) consists in investigating a strongly interacting hot and dense matter, the so-called Quark-Gluon Plasma (QGP). The QGP is formed at extremely high temperatures and/or at high baryon chemical potential. In this medium, quarks are not confined within hadrons and are expected to be asymptoticaly free.

Two variables are of great meaning to characterize the QGP properties and its evolution, namely: the elliptic flow coefficient v_2 and the nuclear modification factors R_{AA} and R_{CP}. Both of these parameters quantify the QGP effects on the transverse momentum spectra of the produced particles. Here, we focus on R_{AA} and R_{CP}, as it is to be obtained from this study in a near future.

1.1 Standard Model

Heavy-ion physics is based on the Standard Model (SM) of particle physics. The SM theory explains three of the four fundamental forces of nature, namely: (i) the electromagnetic force, (ii) the weak interaction and (iii) the strong interaction. SM unites Quantum Chromodynamics (QCD), which explains the strong force, with electroweak theories in a relativistic quantum field theory. Within this framework, six quarks, six leptons, four force-carrying gauge bosons and the Higgs boson constitute the basic building blocks of matter and interactions in the universe. Figure 1.1 shows a schematic of these particles in different groups. The essential difference between quarks and leptons is that quarks experience the strong force, while leptons do not.

1.2 Strong interaction and Quark-Gluon Plasma

QCD describes the interaction between quarks, which is mediated by gluons (bosons). The coupling strength of the interaction is measured with the help of the (running) coupling constant $\alpha_S(Q^2)$, dependent on the momentum transfer Q^2. For large momentum transfer and/or small distances between quarks, we have small values of the coupling

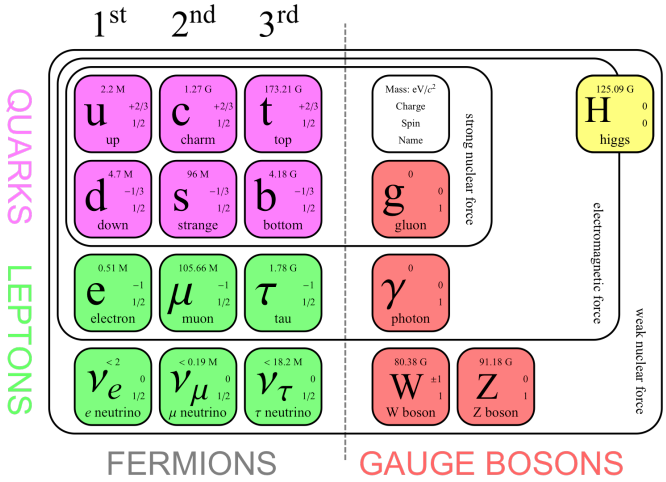

Figure 1.1: Diagram of the elementary particles and interactions described in the Standard Model [1].

constant ($\alpha_S << 1$). In this case, they exhibit asymptotic freedom and processes can be calculated with the aid of perturbative QCD. For small momentum transfer and/or large distances, the interaction strength increases ($\alpha_S \approx 1$) and quarks are confined in color-neutral hadrons. In this scenario, processes can be formulated only with phenomenological models or a first principle theory - lattice QCD.

Lattice QCD predicts a phase transition from quark confinement to a "soup" of colored partons (quarks and gluons) at high temperatures and low or zero high baryon chemical potential (μ_B). The μ_B variable measures the imbalance between baryons and anti-baryons at midrapidity, where the collision takes place. Inside this so-called Quark-Gluon Plasma (QGP), partons have a quasi-free behavior. In addition, lattice QCD also predicts a phase transition corresponding to chiral symmetry restoration at a similar temperature. Both transitions can be observed in Figure 1.2.

QGP probes produced in ultrarelativistic heavy-ion collisions can be divided into two regimes, corresponding to "soft" and "hard" processes. The soft part corresponds to reactions with small momentum transfer, and particles are created in the strongly interacting medium. The hard part corresponds mostly to particles or jets produced during hard scatterings before QGP formation, which are affected or even modified by the medium while trespassing it. Here, the particle energy loss plays a big role. Due to this fact, particles produced during hard processes (generally with $p_T > 2$ GeV/c or large masses, as charm and bottom quarks) are used as probes of the medium properties.

1.2.1 Energy loss mechanisms

The heavy flavor probes produced at the initial hard scatterings after the collision will interact with the QGP by exchanging both energy and momentum [3]. There are two ways through which these particles can lose their energy in the QGP:

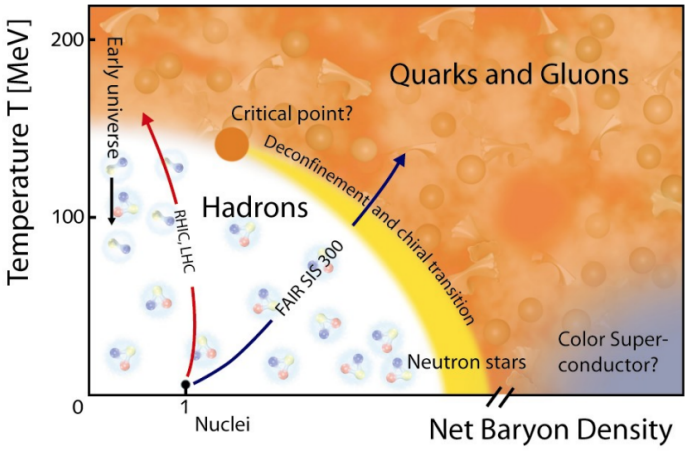

Figure 1.2: Phase transition diagram of QCD matter [2].

1. Collisional processes

2. Radiative processes

In the first case, as the name suggests, hard partons interact with QGP partons via elastic collisions (Figure 1.3a). This is expected to happen mostly at low transverse momentum. In the second case, gluon radiation happens due to exchanged color forces between the heavy flavor quarks and the medium [4] (see Figure 1.3b). Although a definite point corresponding to the transition of one mechanism to the other is not known, radiative energy losses are expected to dominate at high p_T.

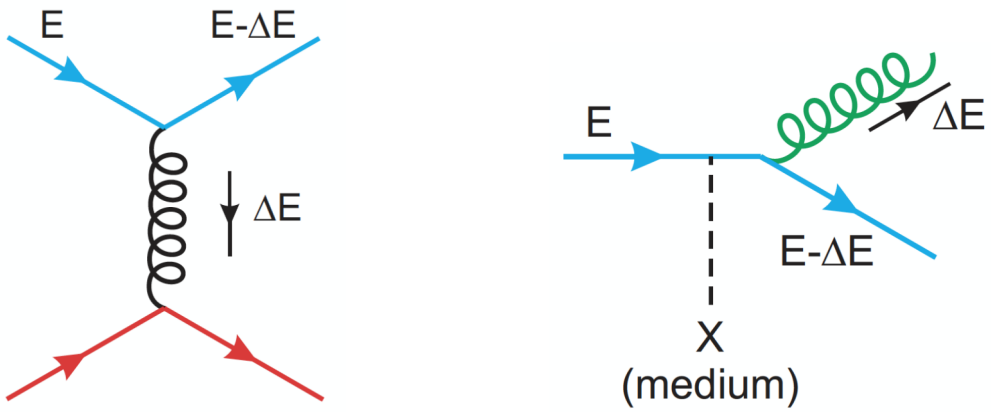

(a) (b)

Figure 1.3: Scheme of (a) collisional and (b) radiative energy loss mechanisms.

For non-central heavy-ion collisions, the overlap geometry of the colliding nuclei exhibits an "almond shape" due to the spatial anisotropy (Figure 1.4). For hard probes

traversing the medium at high p_T ($p_T > 10$ GeV/c) in non-central collisions, a shorter path length in the in-plane direction when compared to the out-of-plane direction results in a lower energy loss, generating non-zero elliptic flow (v_2) of heavy-flavor hadrons. In addition, the energy loss depends on the probe's color and its mass. In the so-called dead cone effect, the radiation of an emitter of mass m and energy E is suppressed at angles below the ratio m/E [5]. Larger quark masses consequently imply in a larger radiation angle limit, and heavy quarks radiate less gluons. This translates to a mass hierarchy in quark energy loss.

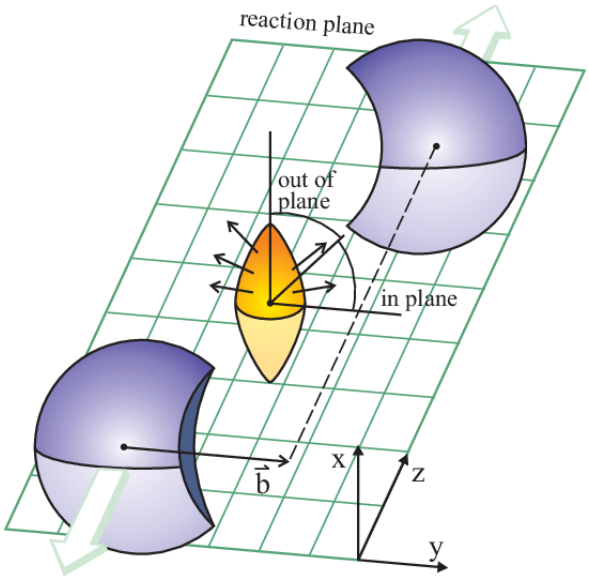

Figure 1.4: Spatial anisotropy in non-central heavy-ion collisions [6].

1.2.2 Nuclear modification factor R_{AA}

As aforementioned, hard probes can be used to study the characteristics of the medium via different processes. These probes need to be produced before the QGP formation and need to interact strongly with the medium. Since charm and bottom quarks are produced during the initial hard scatterings and are also not present in matter before the collision, particles with heavy quark content (D/B mesons) or heavy quark-antiquark bound states (quarkonia) are good candidates to our hard probes. More information about quarkonia can be found in references [7, 8], and more information on D and B mesons is given in section 1.3.

Concerning D and B mesons, there are two approaches to study them: via their direct reconstruction using the hadronic decay channel or via their indirect measurement from a product of the semileptonic decay channel - the heavy-flavor electrons. The decay processes of the D meson is illustrated in Figure 1.5. During year 2017, STAR did not have the Heavy Flavor Tracker (HFT) subdetector installed, and the reconstruction

of secondary vertices of heavy-flavor hadron decays was not possible. Moreover, the semileptonic channel of heavy-flavor meson decays has the most significant branching ratio and is therefore a good alternative. Hence, we use electrons from open heavy flavor hadron decays (HFE) as the probes in this research project.

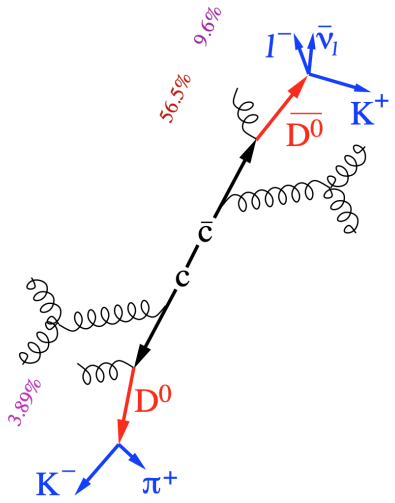

Figure 1.5: Representation of the semileptonic and hadronic decay channels of the D^0 meson [9].

By studying the energy loss of hard probes in the medium, we can investigate the QGP properties. This is accomplished by measuring the nuclear modification factor R_{AA}, introduced in Equation 1.1. R_{AA} compares the yield of particles produced in a heavy-ion collision with a reference pp collision at the same center-of-mass energy, scaled by the number of binary collisions (N_{coll}).

$$R_{\mathrm{AA}}\left(p_{\mathrm{T}}\right)=\frac{1}{\langle N_{coll}\rangle}\frac{dN_{AA}/dp_{\mathrm{T}}}{dN_{pp}/dp_{\mathrm{T}}} \tag{1.1}$$

When data from pp collisions is not available, energy loss can also be measured via the parameter R_{CP} (Equation 1.2), given by the ratio between the yield in central heavy-ion collisions and peripheral heavy-ion collisions, normalized by the number of binary collisions. This is possible because QGP effects in peripheral collisions can be neglected, or the medium might not even be formed. By comparing it to central collisions, we can understand the energy loss of the probe particle.

$$R_{\mathrm{CP}}\left(p_{\mathrm{T}}\right)=\frac{1}{\langle N_{coll}\rangle}\frac{dN_{central}/dp_{\mathrm{T}}}{dN_{peripheral}/dp_{\mathrm{T}}} \tag{1.2}$$

One of the future goals of this project is to calculate the R_{CP} or R_{AA} of electrons from open heavy-flavor decays in heavy-ion collisions at the STAR experiment.

1.3 D and B mesons

Heavy-quark pairs ($b\bar{b}$ and $c\bar{c}$) are produced in pp collisions during a hard process called gluon fusion, described by perturbative QCD [10]. In the case of heavy-ion collisions, the $q\bar{q}$ pairs eventually separate due to charge screening, and quarks might hadronize to heavy-flavor particles, as the D and B mesons [10]. Since strong interactions conserve flavor, the number of charm and bottom quarks in QGP is maintained until hadrons as the D and B mesons decay via weak interaction.

The quark contents of D and B mesons along with their masses and quantum numbers are listed in Table 1.1.

Particle	**Mass MeV/c^2**	**Composition**	$I(J^P)$	**Antiparticle**
D^0	1864.84 ± 0.05	$c\overline{u}$	$1/2(0^-)$	$\overline{D}^0$
D^+	1869.66 ± 0.05	$c\overline{d}$	$1/2(0^-)$	D^-
B^0	5279.65 ± 0.12	$u\bar{b}$	$1/2(0^-)$	$\overline{B}^0$
B^+	5279.34 ± 0.12	$d\bar{b}$	$1/2(0^-)$	B^-

Table 1.1: Mass, composition, quantum numbers and antiparticle of the D and B mesons.

1.4 Current STAR and ALICE results

By comparing the yield of a given particle species in heavy-ion and pp collisions, as well as by comparing the yield in central and peripheral collisions, one can measure how the produced particles are affected by the QGP. In order to understand the partonic energy loss in the medium, STAR and ALICE already studied the non-photonic electron production at different collision types, energies and centralities.

Older and more recent results published by the STAR Collaboration [11, 12, 13, 14, 15] showed a large yield suppression of NPE in $Au+Au$ collisions at $\sqrt{s_{NN}} = 200$ GeV when compared to pp data at the same energy (see Figure 1.6a). This happened mainly for intermediate to high p_T, indicating a strong suppression of b quarks via radiative energy loss.

Recent results obtained by the ALICE Collaboration [16, 17] showed a similar behavior for $Pb+Pb$ collisions at $\sqrt{s_{NN}} = 2.76$ TeV and $\sqrt{s_{NN}} = 5.02$ TeV, with a weakening suppression for decreasing centralities (Figure 1.6c). This also corroborates with the hypothesis of a medium induced energy loss of the heavy flavor partons.

STAR $Au+Au$ results at $\sqrt{s_{NN}} = 62.4$ GeV although showed no meaningful suppression of the NPE yield (Figure 1.6b) when comparing to pp collisions, indicating a change in the medium behavior between the two different collision energies [14]. In this niche, our NPE analysis at $\sqrt{s_{NN}} = 54$ GeV might provide a glimpse of the change of the fluid dynamics for decreasing collision energies.

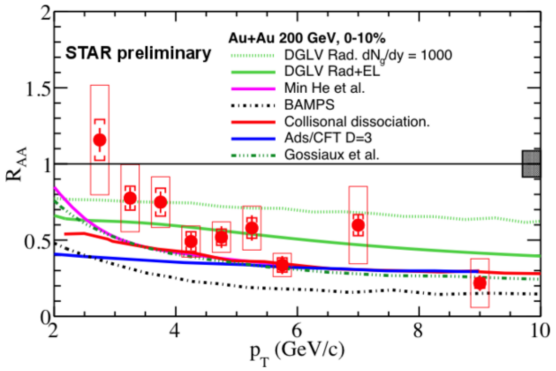

(a) R_{AA} vs p_T for STAR $Au + Au$ collisions at $\sqrt{s} = 200$ GeV showing strong yield suppression at high p_T [14].

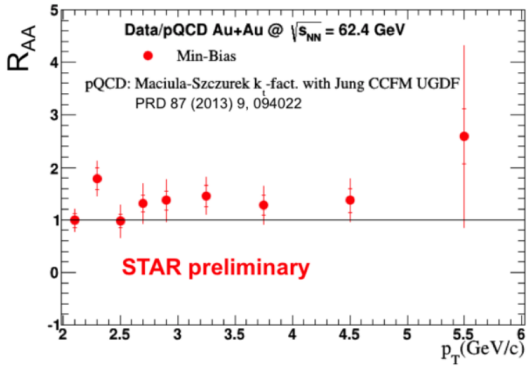

(b) R_{AA} vs p_T for STAR Au+Au collisions at $\sqrt{s} = 62.4$ GeV showing no meaningful yield suppression [14].

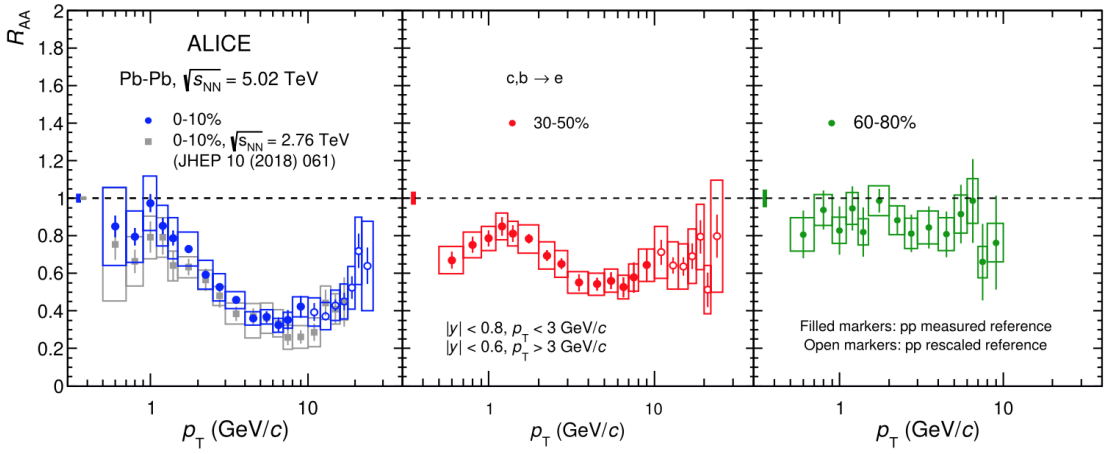

(c) R_{AA} vs p_T for ALICE Pb+Pb collisions at $\sqrt{s} = 5.02$ TeV showing strong yield suppression at high p_T [17].

Figure 1.6: STAR and ALICE results for R_{AA} vs p_T of non-photonic electrons.

Chapter 2

The STAR Experiment

The Relativistic Heavy-Ion Collider (RHIC) is a high energy particle collider located in Upton, New York. RHIC has the capability of colliding different ion species at different beam energies. Studies were already carried out using $p+p, d+Au, Cu+Cu, Cu+Au, Au+Au$ and $U+U$. Moreover, the RHIC Beam-Energy-Scan (BES) performed $Au+Au$ collisions with energies per nucleon pair between 7.7 GeV and 200 GeV. The BES program brought about relevant results that characterize the QGP and QCD matter phase transition, including beam-energy dependent flow for different particles and antiparticles [18], change of the proton directed flow dependent on beam energy [19], a probable absence of phase transition at lower beam energies [20] and the particle production and freeze-out conditions in the search of a QCD critical point [21].

Experiments at RHIC are conducted in the different interaction points of its storage ring, including STAR. STAR (Solenoidal Tracker at RHIC) is a detector built to investigate the QGP and to study the origin of the proton spin. It is formed by a system of subdetectors capable of identifying different particle species, resulting from ultrarelativistic heavy-ion or nucleon collisions. Figure 2.1 depicts STAR with the indicated subsystems that were used in this study.

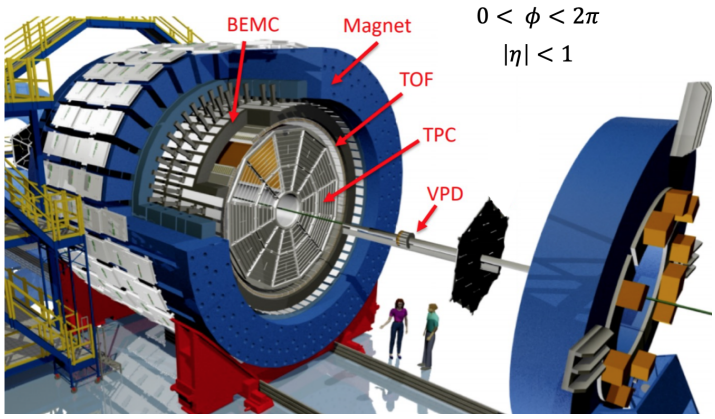

Figure 2.1: Scheme of the STAR detector with its subsystems. Adapted from [22].

2.0.1 Vertex Position Detector (VPD)

The Vertex Position Detector (VPD) [23] consists of two assemblies of nineteen detectors positioned 5.7m away from the interaction region at the east and west sides of the STAR Experiment. The nineteen detectors consist of a Pb converter and a plastic scintillator, read out by a photomultiplier tube. Each side of the VPD contributes with a maximum of 19 time measurements per event and covers a pseudorapidity range of $4.24 < |\eta| < 5.1$. Time information from VPD is used to measure the position of the primary vertex and also to serve as a Minimum Bias trigger to the STAR Experiment. At $Au + Au$ collisions at $\sqrt{s_{NN}} = 200$ GeV for example, the VPD enables a start time resolution of tens of picoseconds and a spatial resolution of the primary vertex location of $\approx$ 1cm [23]. The VPD is represented in Figure 2.2.

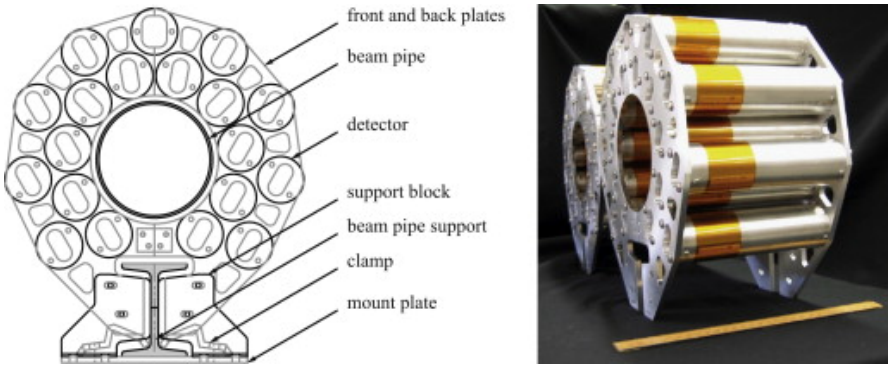

Figure 2.2: Scheme of the transversal section and side view picture of the Vertex Position Detector [23].

2.0.2 Time Projection Chamber (TPC)

Covering full azimuth ($\phi < 2\pi$) and a pseudorapidity range of $|\eta < 1|$, the Time Projection Chamber (TPC) [24] is the main detector for particle identification at STAR. It is employed to measure charged particle momentum and ionization energy loss and to reconstruct the primary vertex. A scheme of the detector is depicted in Figure 2.3.

The TPC consists of a large chamber filled with P10 gas (10%Ar and 90%CH_4), submitted to a magnetic field of $B = 0.5$T. While a conductive membrane in the middle of the detector plays the role of the cathode, both ends of the detector act as anodes at a high voltage. When charged particles traverse the gas filled region, they ionize the gas. Electrons produced during the ionization process drift towards the endcaps in an electric field of $\approx$ 135V/cm, and are read with the help of readout pads in Multiwire Proportional Chambers.

As the charged particles travel through the magnetic field, their trajectories are bent according to their masses due to the Lorentz force. The transverse momentum (p_T) of the particles is then measured based on the xy coordinates of the particle tracks. The

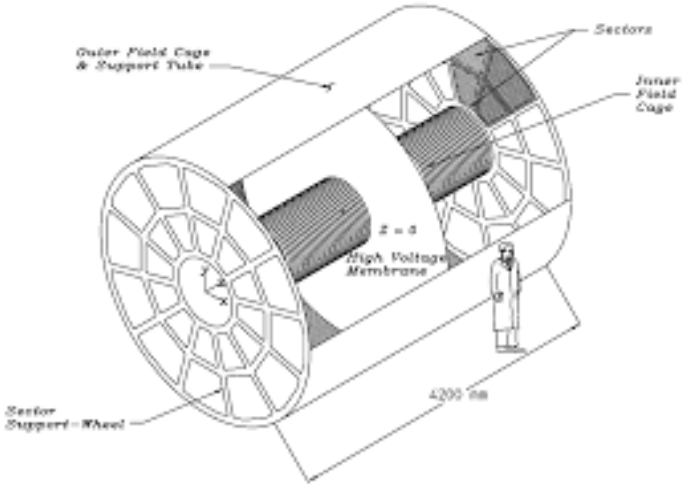

Figure 2.3: Representation of the TPC detector [24].

coordinate z, on the other hand, is measured with the time taken for the electrons to drift towards the cathodes.

Charged particles also lose energy by ionizing the gas when traversing the TPC chamber. This specific ionization energy loss enables us to distinguish between different particle species, according to the Bethe-Bloch formula (Equation 2.1):

$$-\frac{dE}{dx} = Kz^2\frac{Z}{A}\frac{1}{\beta^2}\frac{1}{2}\ln\frac{2m_ec^2\beta^2\gamma^2T_{\max}}{I^2} - \beta^2 - \frac{\delta}{2} - 2\frac{C}{Z} \tag{2.1}$$

In Equation 2.1, Z stands for the atomic number and A for the atomic mass, $\beta = (v/c)$ corresponds to the velocity of the electron and m_e to the electron mass, c is the speed of light, I is ionization potential of the medium, $\gamma = \frac{1}{\sqrt{1-\left(\frac{v}{c}\right)^2}}$ is the Lorentz factor and $T_{\max}$ the maximum energy transfer. The parameters δ and C are, respectively, the density and shell corrections. The density effect emerges due to polarized atoms along the path of the incoming particle. The shell effect is significant only when the incident particle has a velocity comparable to the orbital velocity of the bound electrons. In Equation 2.1, K depends on the detector materials, on the Avogadro constant (N_A) and on the classical electron radius r_e according to Equation 2.2.

$$K = 4\pi N_A r_e^2 m_e c^2 \rho z^2 \tag{2.2}$$

2.0.3 Time of Flight (TOF)

The Time of Flight (TOF) [25] detector at STAR covers the full azimuthal angle ($\phi < 2\pi$) and a pseudorapidity range of $|\eta| < 1$. It is formed by 120 trays, each of them based on 32 multi-gap resistive plate chambers (MRPCs). A MRPC corresponds to a stack of parallel resistive plates with high resolution for time measurement ($t > 100$

ps). Intermediate plates inside the MRPC structure create gaps to be filled with gas. A high voltage applied to the MRPC electrodes submits the system to a high electric field. When charged particles traverse the system, particle avalanches are produced. These avalanches induce signals in readout pads. TOF distinguishes between charged particles by measuring the stop time of the incoming particle with a subsequent subtraction of its start time (provided by the VPD), thus obtaining the particle time of flight.

2.0.4 Barrel Electromagnetic Calorimeter (BEMC)

The Barrel Electromagnetic Calorimeter at STAR [26] is a lead-scintillator calorimeter used to identify electrons and photons at high energies ($E > 1$ GeV). The STAR BEMC covers the full azimuthal angle and a pseudorapidity range of $|\eta| < 1$, matching the TPC acceptance. It consists of 120 modules of 40 towers each, resulting in 4800 towers. All towers point to the interaction region, covering full azimuth. A scheme of the BEMC at STAR is depicted in Figure 2.4.

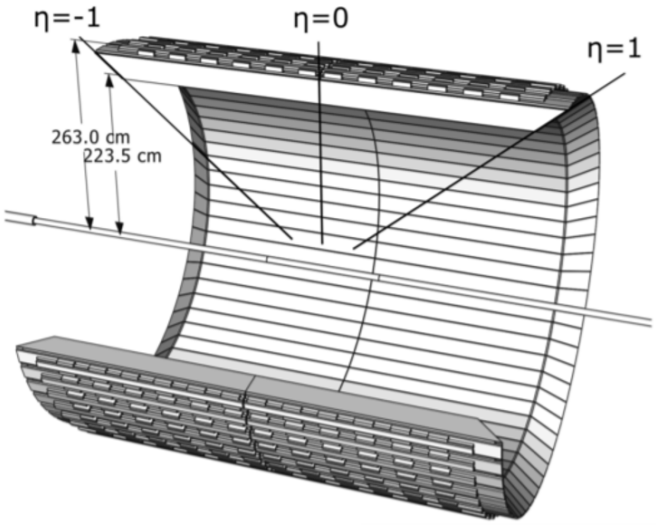

Figure 2.4: Scheme of the Barrel Electromagnetic Calorimeter (BEMC)[27].

Each BEMC module corresponds to a stack of 20 layers of lead and 21 layers of scintillators, with a Barrel Shower Maximum Detector (BSMD) embedded at a depth of 5 radiation lengths to provide a better spatial resolution of the particle showers. A scheme of a BEMC module is depicted in Figure 2.5, together with the wire layers scheme that provide a 2D image of the electromagnetic showers.

The BEMC, as a conventional electromagnetic calorimeter, is built to absorb electrons and photons in the bulk of the lead-scintillator modules. The interaction of the traversing particles with the calorimeter creates electromagnetic showers due to e^+e^- pair creation and Bremsstrahlung photon production. According to the parameters of

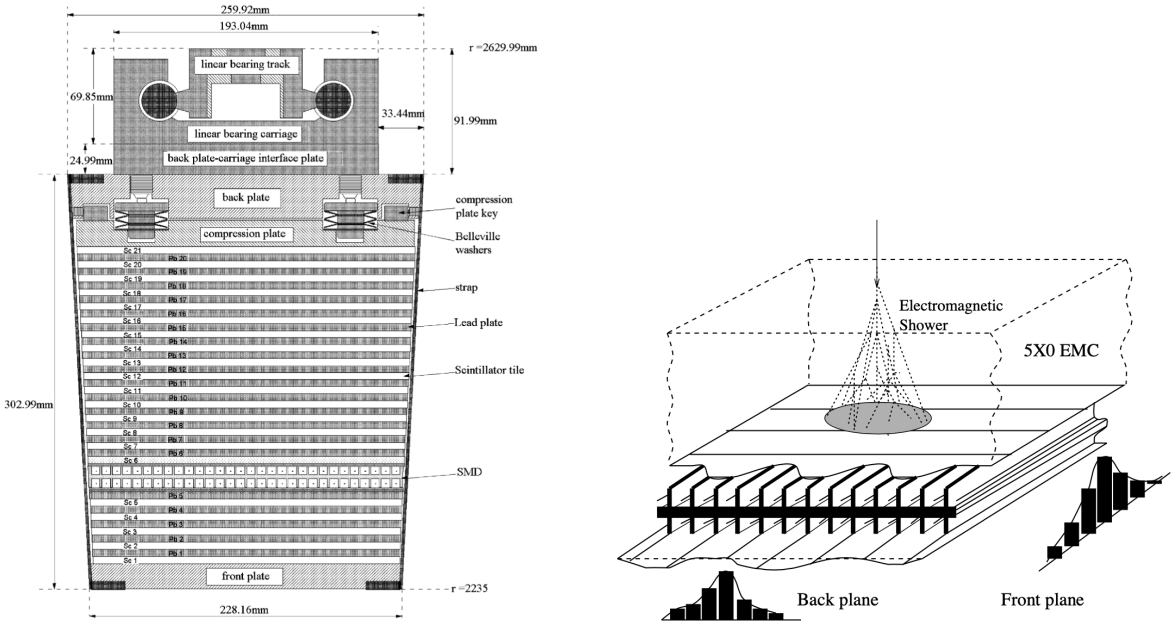

(a) (b)

Figure 2.5: (a) Scheme of one BEMC module showing the stack of lead and scintillator layers and the BSMD [26]. (b) Display of the wire layers scheme that provide the BEMC with 2D spatial resolution [26].

the shower shape, one can extract the energy and direction of the initial particle. Moreover, according to the percentage of the deposited energy, one can distinguish between the produced particles. Electrons, for instance, deposit almost all their energy on the calorimeter and are therefore easily detected.

Chapter 3

Data Analysis

3.1 Non-photonic electron measurement

All electrons identified in one specific event are named inclusive electrons, and they are classified in two general categories: the photonic electrons (PE) and the non-photonic electrons (NPE). In more detail, the main electron sources of both categories with the respective branching rations (B.R.) are given as follows [28]:

1. Photonic electrons (PE)
   (a) Dalitz decays
      - $\pi^0 \to e^+e^-\gamma$ B.R. $(1.1.74 \pm 0.035)\%$
      - $\eta \to e^+e^-$ B.R. $(0.69 \pm 0.04)\%$
   (b) Gamma conversions from di-gamma decays
      - $\pi^0 \to \gamma\gamma$ B.R. $(98.823 \pm 0.034)\%$
      - $\eta \to \gamma\gamma$ B.R. $(39.41 \pm 0.20)\%$
      - Direct photons
2. Non-photonic electrons (NPE)
   (a) Heavy-flavor decays
      - $D^+ \to e^+$ semileptonic B.R. $(16.07 \pm 0.30)\%$
      - $D^0 \to e^+X$ B.R. $(6.49 \pm 0.11)\%$
      - $B^+ \to e^+$ semileptonic B.R. $(10.8 \pm 0.4)\%$
      - $B^0 \to e^+X$ B.R. $(10.1 \pm 0.4)\%$
   (b) Drell-Yan and heavy quarkonia contributions
   (c) Vector mesons dielectron decays
   (d) Single electron background sources

As mentioned in section 1.2.2, we are interested in the identification of electrons produced in the semileptonic decays of heavy flavor mesons. The energy loss of these hard probes will be used to characterize the QGP in our study. As heavy-flavor electrons do not originate from photonic sources, they are classified as NPE.

The usual technique employed by the STAR Collaboration to reconstruct NPE constitutes in obtaining the corrected yield of photonic electrons and subsequently in subtracting it from the inclusive electron sample. The PE yield correction is performed based on simulation of the STAR subdetectors. These simulations constitute future steps in our analysis.

Besides the corrected yield of PE, one also needs to consider the purity of the inclusive electron sample (ϵ_{purity}) due to p_T-dependent hadron contamination to obtain the NPE. We are currently working on the purity estimation, and some initial results are presented in section 4.3.

In summary, after the aforementioned steps are followed, the NPE yield is obtained using the following equation:

$$N_{NPE} = \frac{N_{incl} \cdot \epsilon_{purity} - N_{PE,corrected}}{\epsilon_{tot}} \tag{3.1}$$

In Equation 3.1, N_{NPE}, N_{incl} and $N_{PE,corrected}$ represent the non-photonic electron yield, the inclusive electron yield and the corrected photonic electron yield, respectively. Here, $N_{PE,corrected}$ is given by $N_{PE,corrected} = N_{PE}/\epsilon_{PE}$, where N_{PE} is the uncorrected photonic electron yield and ϵ_{PE} the efficiency of PE reconstruction, which will be obtained from simulations. Also in Equation 3.1 is the parameter ϵ_{tot}, representing the overall electron efficiency.

Based on the outputs of the previous calculation, one can obtain the nuclear modification factors R_{AA} and/or R_{CP} to investigate the energy loss of our hard probes in the medium.

One of the first steps in this analysis is to obtain the uncorrected yield of inclusive electrons, N_{PE}. For this purpose, we apply a sequence of cuts in the measured tracks followed by a statistical approach. For the electron identification, we use the available information from TPC, TOF and BEMC detectors. Details about the applied cuts are given in section 3.4. The statistical method is explained in the next section.

3.2 Photonic electron tagging

Photonic electrons are identified by analyzing the invariant mass spectrum of electron-positron pairs (e^+e^-). To obtain ee pairs in a given event, we combine a primary (tagged) electron candidate with all possible partner electrons in a given event. A representation of this process is given in Figure 3.1.

Since PE come mostly from photon conversions, they produce a peak in the low mass region of the invariant mass plot of e^+e^- pairs. Other pairs that do not come from PE

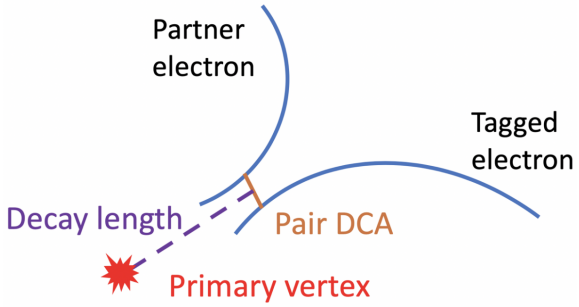

Figure 3.1: Pairing of tagged (inclusive) electrons with partner electrons for the reconstruction of photonic electrons.

will produce a combinatorial background. To subtract the combinatorial background from the e^+e^- mass spectrum, we apply the unlike-like sign technique (UL-LS).

In the (UL-LS) technique, the signal+background curve in the invariant mass spectrum of ee pairs corresponds to unlike-sign pairs e^+e^- (UL), while the combinatorial background can be described as a sum of like sign pairs (LS), e^+e^+ and e^-e^-, in a given event. Cuts on the dielectron pairs are listed in section 3.5. To obtain the signal of the photonic electrons, we subtract the LS pairs from the UL pairs. Figure 3.2 displays the invariant mass distribution obtained in our analysis. This result, after an appropriate signal correction, will be used to obtain the NPE yield in future steps of this analysis.

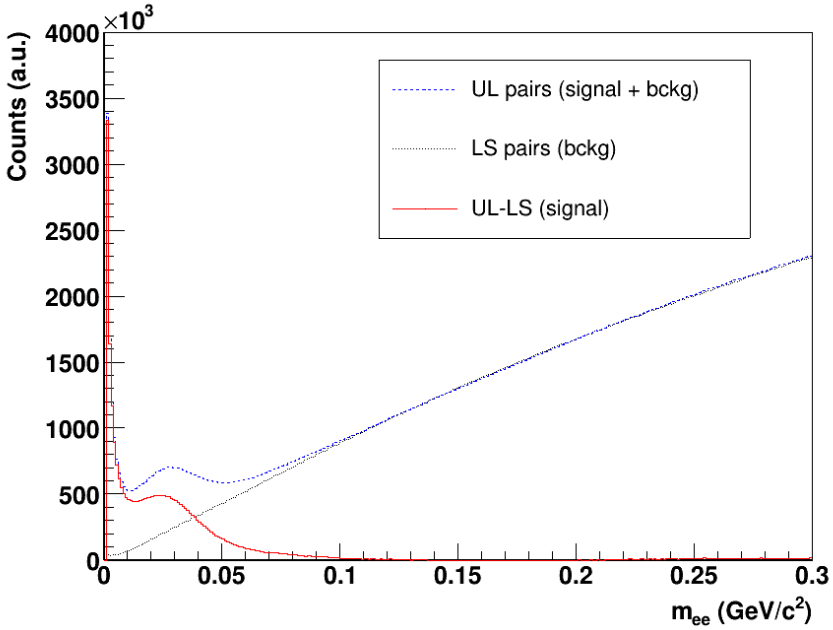

Figure 3.2: Invariant mass distribution of ee pairs. Background of the distribution is reconstructed using the LS technique.

3.3 Dataset and event selection

This research task analyses minimum bias triggered data from $Au + Au$ collisions collected during year 2017, at a center-of-mass energy $\sqrt{s_{NN}} = 54$ GeV in a centrality range of $0 - 60\%$. Altogether, this dataset comprised ca. 1.35 B events before event selection and ca. 580 M events after event selection.

The search for the non-photonic electrons starts with the event cuts. Cuts on this level ensure that bad events are discarded, mainly by restricting the position of the primary vertex. After selecting the events, cuts are applied on the track level, with a subsequent identification of inclusive electrons. Following, loosened cuts are applied to the partner electrons, increasing the reconstruction efficiency (see section 3.4.3). Finally, cuts are applied on the di-electron pairs in order to identify the photonic electrons (see section 3.5).

In order for us to analyse only good quality events, cuts are applied on the position of the primary vertex. All event cuts are displayed in Table 3.1. The first cut, applied on $|V_r|$, ensures that the event happens within the beam pipe. Following, the cut on $|V_z|$ requires that collisions happen inside the TPC, with a uniform acceptance and a low background related to photon conversions in the detector material. Cuts on $|V_x, V_y, V_z|$ are necessary to reject badly reconstructed vertices. Lastly, the cut $|V_{z,vpd} - V_z|$ removes pile-up events.

Event cuts	
$\lvert V_r \rvert$	< 2 cm
$\lvert V_z \rvert$	< 35 cm
$\lvert V_{z,vpd} - V_z \rvert$	< 3 cm
$\lvert V_x, V_y, V_z \rvert$	$> 10^{-5}$ cm

Table 3.1: Event cuts

3.4 Electron identification

After the event selection, cuts are applied at the track level to choose the tracks of interest. The identification of inclusive electrons is then accomplished with the information from TOF, BEMC and TPC. Track and electron identification cuts are applied differently in the case of inclusive (tagged) and partner electrons: partner electron cuts are less strict in order to improve reconstruction efficiency. These steps are explained in more detail in the next subsections.

3.4.1 Track selection

Cuts are applied at the track level mainly to select good quality tracks, but also to improve track reconstruction efficiency and purity. The |gDCA| cut (global Distance of Closest Approach), for example, selects only tracks that come from the primary vertex. This selects heavy-flavor electrons, which have a very short lifetime. The $|\eta| > 0.8$ cut guarantees a uniform track acceptance. nHitsFit corresponds to the number of TPC hit points, which shall be greater than 20 for a good momentum resolution. nHitsFit2Poss corresponds to the ratio nHitsFit/nHitsMax, and shall be larger than 0.52 to remove split tracks. Finally, nHitsDedx corresponds to the number of TPC hits used to measure the particle ionization energy loss, which must be of at least 15 to improve the dE/dx resolution.

Track cuts	
p_T	> 0.2 GeV/c
nHitsFit	> 20
nHitsDedx	> 15
nHitsFit2Poss	> 0.52
$\|\eta\|$	< 0.8
|gDCA|	< 1.5 cm

Table 3.2: Track cuts

3.4.2 Inclusive electrons

Electron identification with TPC

For TPC particle identification, we base ourselves on a parameter derived from the particle energy loss. This parameter, called $n\sigma_x$, relates the measured and the expected energy loss in the TPC gas for a given particle species (x) according to equation 3.2, where $\sigma_{dE/dx}$ is the dE/dx resolution of the TPC:

$$n\sigma_x = \frac{1}{\sigma_{dE/dx}} \ln \frac{\langle dE/dx \rangle_{measured,x}}{\langle dE/dx \rangle_x} \tag{3.2}$$

The cuts applied to identify the electrons and reduce hadron contamination (mainly pions) is given in table 3.3.

Electron identification with TOF

For electron identification using TOF, we apply cuts on the particle velocity. Since electrons are expected to have their velocity close to the speed of light, their beta

parameter ($\beta = c/v$) lies close to unit. By applying the cut $|1/\beta - 1| < 0.025$, we can distinguish electrons from hadrons until the point which all the particles have a velocity close to c.

Electron identification with BEMC

An important step when dealing with BEMC information and cuts is a sanity check to investigate whether some performance problems were present during the runs. As this QA wasn't ready for 54 GeV data before this project, we decided to investigate the possible appearance of hot towers during data acquisition - one of the main issues when dealing with the calorimeter. The results are introduced in Section 4.1.

For particle identification using BEMC, cuts are applied on the energy-to-momentum ratio E/p (alternatively on p/E). Depending on the type of collision and amount of background, one chooses between the tower energy (E_{tow}) or cluster energy (E_{cl}) to calculate E/p. As particles may deposit their energy not only in a single tower, the energy of a cluster (E_{cl}) is generally taken into consideration. A cluster is characterized by a tower with the highest deposited energy and its adjacent towers.

Electrons are expected to have an E/p ratio around unit, since they essentially deposit all their energy in the BEMC. For this reason, we apply a cut at an E/p interval which includes unit. An estimate on the best cut interval and an analysis on which energy (whether E_{cl} or E_{tow}) to use were performed. The results are presented in Section 4.2. First, we elected a cut of $0.6 < E_{tow}/p < 1.25$. This provides us a larger amount of statistics at the beginning in order to improve the cut and work on its purity in a second step.

$e^{\pm}$ **identification cuts**
if $\|p\| > 0.8 \rightarrow 0 < n\sigma_{el} < 2$
if $\|p\| < 0.8 \rightarrow (2.5 \cdot p - 2.8) < n\sigma_{el} < 2$
$\|1 - \frac{1}{\beta}\| < 0.025$
$0.6 < E_{tow}/p < 1.25$

Table 3.3: Cuts applied for the identification of inclusive electrons.

To show how the aforementioned electron identification cuts operate on the tracks, Figure 3.3 displays the $1/\beta$ vs. p, $n\sigma_{el}$ vs. p and the E_{tow}/p vs. p_T distributions before and after TOF, BEMC and TPC cuts were applied (both after event and track quality cuts).

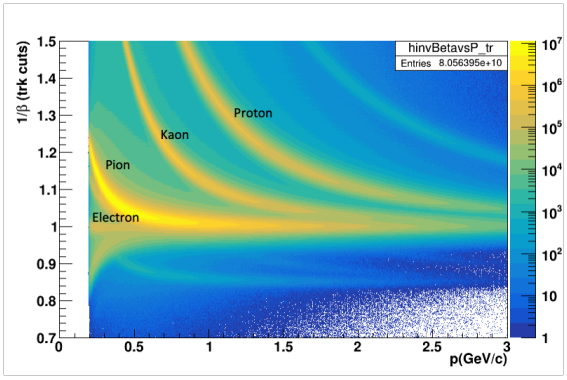

(a) $1/\beta$ vs p distribution before electron ID.

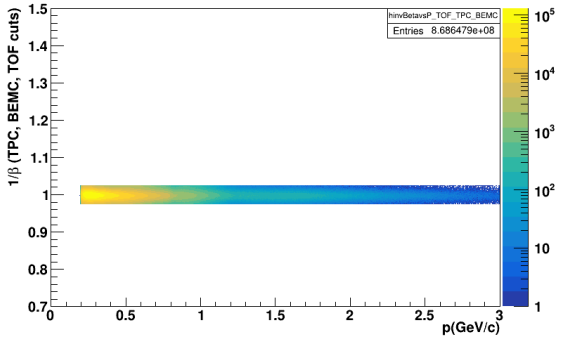

(b) $1/\beta$ vs p distribution after electron ID.

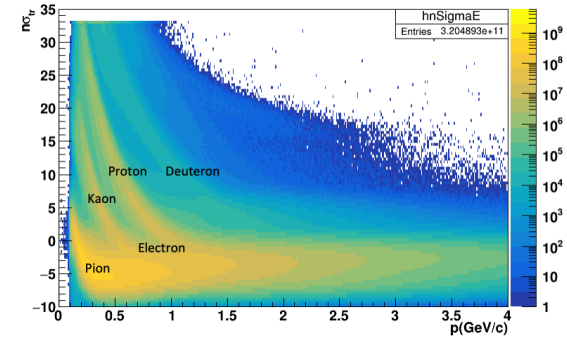

(c) $n\sigma_{el}$ vs p distribution before electron ID.

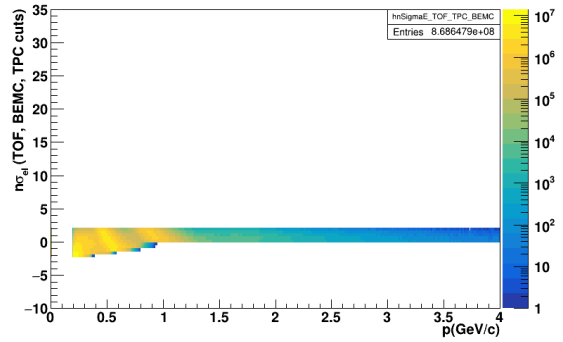

(d) $n\sigma_{el}$ vs p distribution after electron ID.

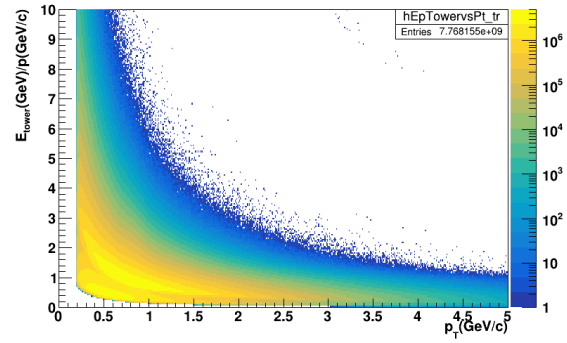

(e) E_{tow}/p vs p_T distribution before electron ID.

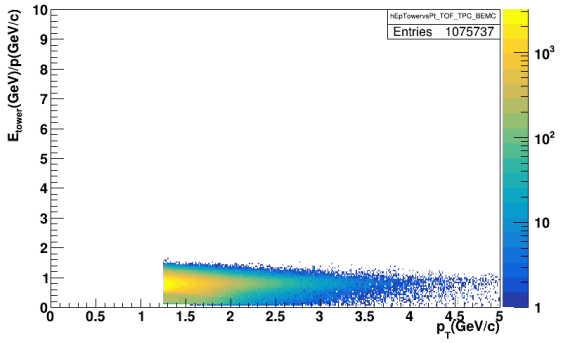

(f) E_{tow}/p vs p_T distribution before electron ID.

Figure 3.3: Histograms on the left display track distributions just after track quality cuts and on the right just after TPC, TOF and BEMC identification cuts.

3.4.3 Partner electrons

After inclusive (tagged) electron candidates have been chosen, we need to select the partner electron candidates for photonic electron identification, which are used in a tag-and-probe method to study the efficiency of the detectors. These do not need the same strict cuts, as the electron reconstruction efficiency could decrease significantly. We rather have better efficiency and "worse" purity for the PE reconstruction. All partner electrons are required to be global tracks and to obey the cuts displayed in Table 3.4. As one can see, some track selection cuts are applied followed by only a loosener TPC $n\sigma_{el}$ cut. BEMC and TOF cuts are not implemented.

Track cuts	
gp_T	> 0.25 GeV/c
nHitsFit	> 15
$\lvert\eta\rvert$	< 1.0
$n\sigma_{el}$	< 3.0

Table 3.4: Partner electron cuts.

3.5 Di-electron pair cuts

After both tagged and partner electrons are selected, they are combined in pairs of opposite charge. After plotting their invariant mass (Figure 3.2) and after subtracting the combinatorial background with the help of the like-sign technique (see Section 3.2), photonic electrons are selected if they pass the following cuts:

- pair DCA < 1 cm
- $m_{e^+e^-} < 0.1$ GeV/c^2

Chapter 4

Results & Discussion

4.1 Hot Towers

Hot towers are characterized as BEMC towers that fire more often then the average of all towers during a specific run. This effect can be detected if we investigate a histogram which relates the number of tower hits and the tower ID. By calculating the average number of hits and allowing a 3σ or 5σ deviation, towers which exceed the nHits are marked as hot. This analysis needs to be performed for every run in our data sample. By rejecting hot towers, we improve the quality of the BEMC data and hence of our electron candidates.

In Figure 4.1a, one can observe that some towers fired more often than the average, far above the 5σ line limit. Meanwhile, figure 4.1b depicts a normal BEMC behavior, with no significant deviations of the number of hits. After all runs and towers are analyzed, we reject information coming from hot towers during the runs in which they fired about 25% more often then the average.

Table 4.1 shows all towers marked as hot according to the runs and to the 5σ tolerance. This information can be used further in other analysis of the STAR Collaboration that employ BEMC in the same dataset.

Tow ID	**Run #**
1900	18161026, 18161027, 18161028, 18161029, 18161030, 18161031, 18161032, 18161033
672	18162045, 18162046, 18162047, 18162048, 18162049, 18162051, 18162052, 18162053
297	18169008, 18169009, 18169010, 18169011, 18169012, 18169013, 18169017, 18169014, 18169015, 18169016, 18169017, 18169018

Table 4.1: Hot Towers during runs.

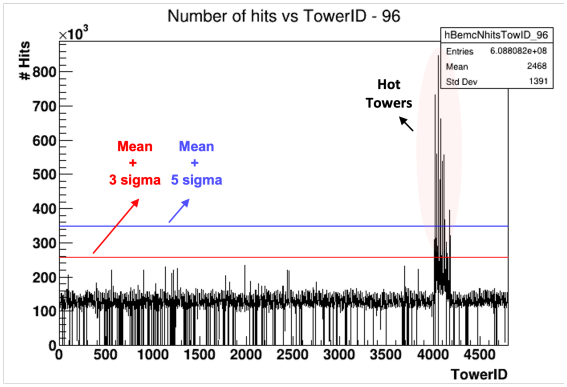

(a) BEMC hot towers above 5σ line.

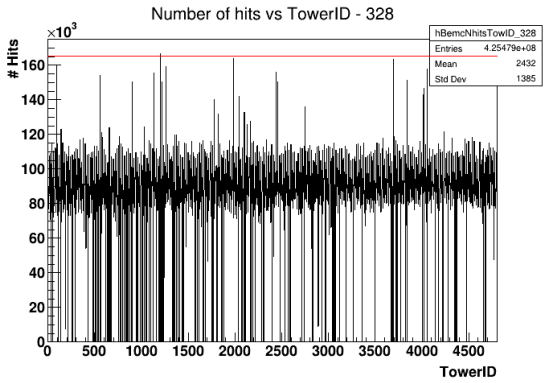

(b) Regular BEMC behavior of BEMC towers.

Figure 4.1: Number of BEMC tower hits vs. tower ID for (a) run 18156014 and (b) run 18163026.

4.2 Purity of the E/p cut

To estimate the best cut on the E/p ratio, including whether to consider tower or cluster information, we analyzed the percentage of contamination of hadrons in different p_T intervals, for different applied cuts. Here, we considered pions as the main source of the hadron contamination. We applied a strict $n\sigma_\pi$ cut to identify the pions within our tracks, and subsequently obtained the E/p distribution for those hadrons. By normalizing this spectrum within the region $0.15 < E/p < 0.6$, we could subtract the pion contamination out of the distribution of the electron candidates ($E/p_{(el)}$), obtaining $E/p_{(el-h)}$. E/p histograms used for the purity estimation for cluster and tower energies are displayed in Figures 4.2, 4.3, 4.4 and 4.5. The blue lines represent the electron candidates after TOF and TPC cuts ($E/p_{(el)}$), and the black lines refer to the pion candidates. The red lines correspond to the electron candidates after the subtraction of the normalized pions ($E/p_{(el-h)}$). The purity is estimated by calculating the ratio $E/p_{(el-h)}/E/p_{(el)}$, and is represented in Figure 4.6.

By observing Figure 4.6, one can notice that the purity is poor at low p_T in both cases as expected: BEMC is employed for particle identification mainly at intermediate to high p_T. Another feature of the purity that can be observed in Figure 4.6 is that it decreases with increasing p_T at high $p_T > 3$ GeV/c. This is due to the increasing pion contribution with the relativistic rise in dE/dx. By comparing figures 4.6a and 4.6b, we conclude that using tower energy gives higher purity than cluster energy. Although E_{cl} is commonly used to calculate the E/p ratio in $p+p$ collisions, it does not represent the best choice in the case of this study due to the larger background in heavy-ion collisions.

As a starting point, we decided to apply the cut $0.6 < E_{tow}/p < 1.25$, which enables us to have more statistics and reasonable purity.

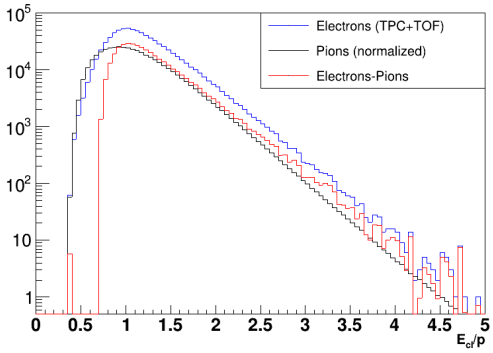

(a) $1.25 < p_T < 1.5$ GeV/c

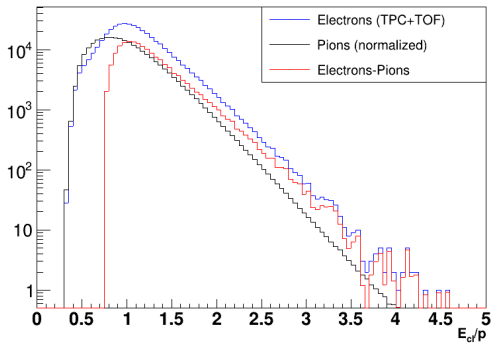

(b) $1.5 < p_T < 1.75$ GeV/c

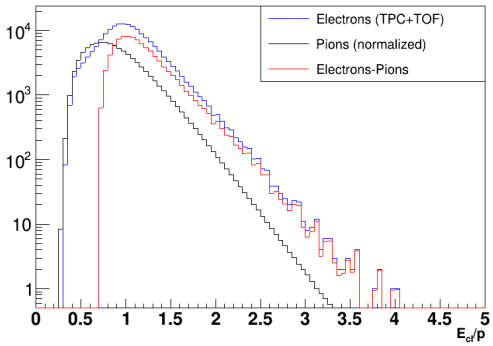

(c) $1.75 < p_T < 2.0$ GeV/c

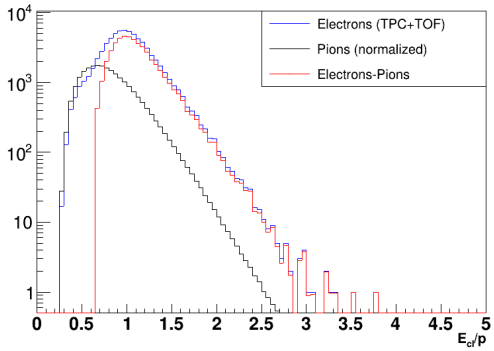

(d) $2.0 < p_T < 2.25$ GeV/c

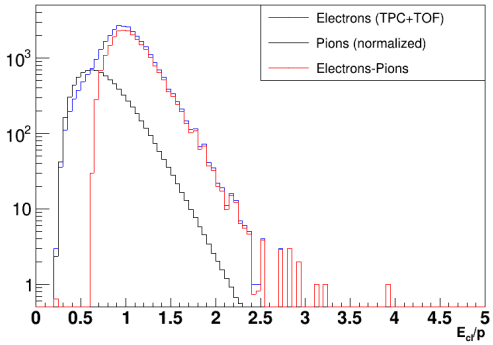

(e) $2.25 < p_T < 2.5$ GeV/c

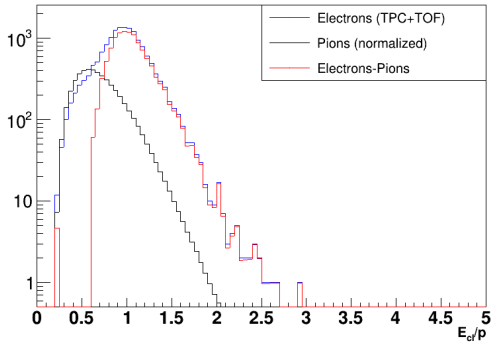

(f) $2.5 < p_T < 2.75$ GeV/c

Figure 4.2: E_{cl}/p vs p_T projections for electron cluster energy, normalized pion tower energy and electrons-normalized pions tower energy.

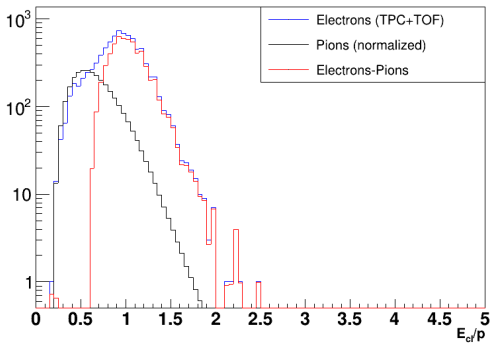

(a) $2.75 < p_T < 3.0$ GeV/c

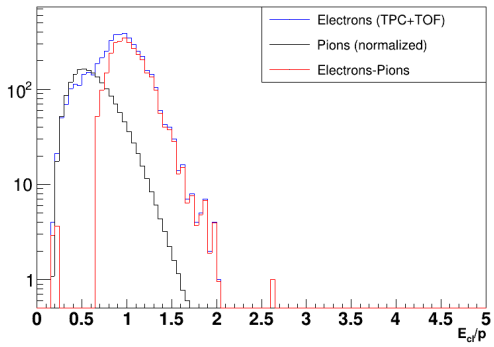

(b) $3.0 < p_T < 3.25$ GeV/c

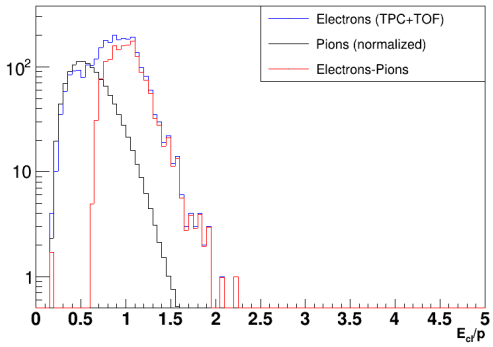

(c) $3.25 < p_T < 3.5$ GeV/c

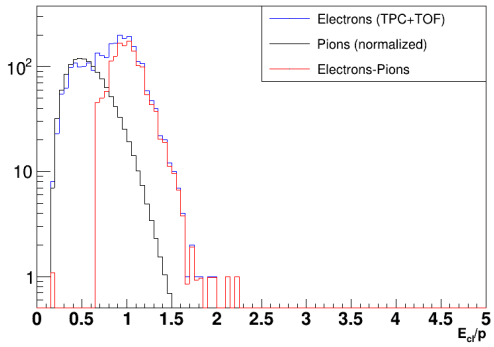

(d) $3.5 < p_T < 4.0$ GeV/c

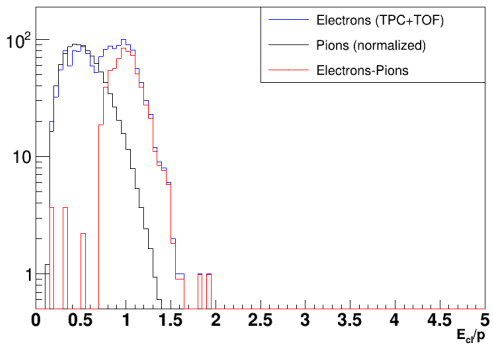

(e) $4.0 < p_T < 5.0$ GeV/c

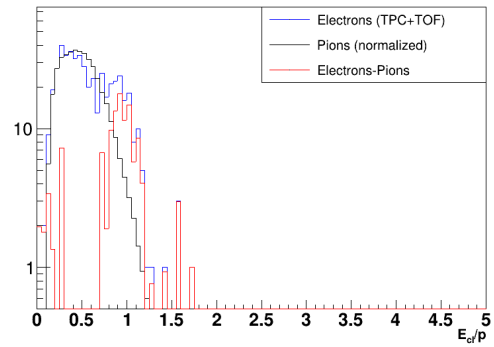

(f) $5.0 < p_T < 6.0$ GeV/c

Figure 4.3: E_{cl}/p vs p_T projections for electron cluster energy, normalized pion tower energy and electrons-normalized pions tower energy.

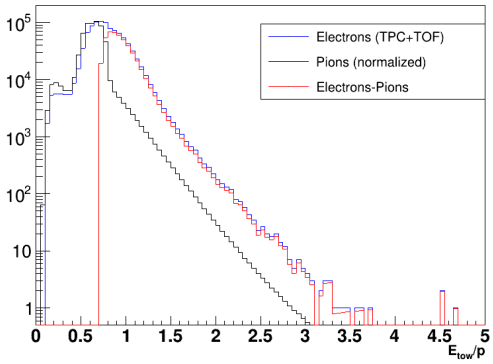

(a) $1.25 < p_T < 1.5$ GeV/c

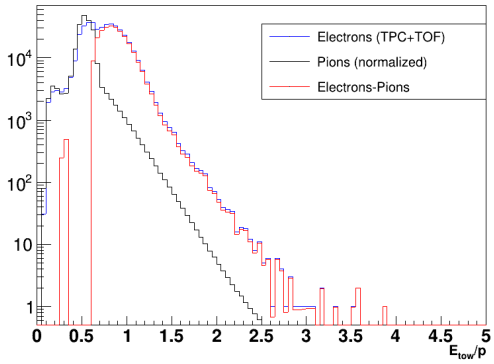

(b) $1.5 < p_T < 1.75$ GeV/c

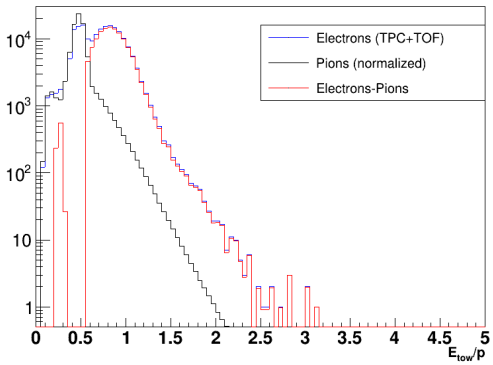

(c) $1.75 < p_T < 2.0$ GeV/c

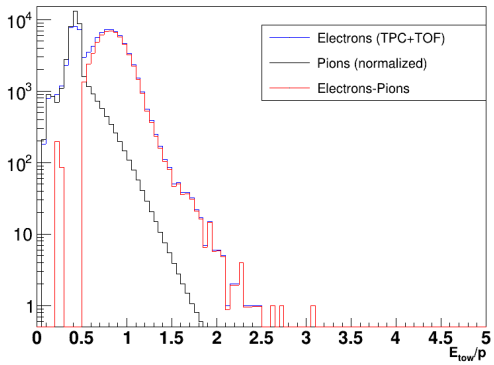

(d) $2.0 < p_T < 2.25$ GeV/c

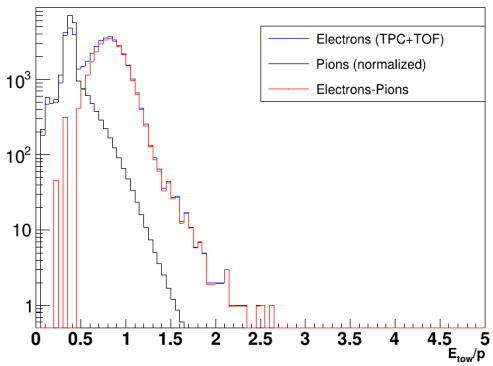

(e) $2.25 < p_T < 2.5$ GeV/c

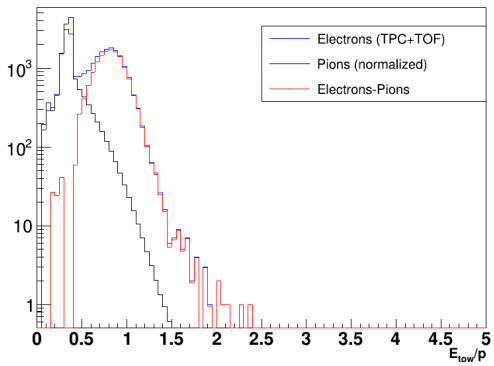

(f) $2.5 < p_T < 2.75$ GeV/c

Figure 4.4: E_{tow}/p vs p_T projections for electron tower energy, normalized pion tower energy and electrons-normalized pions tower energy.

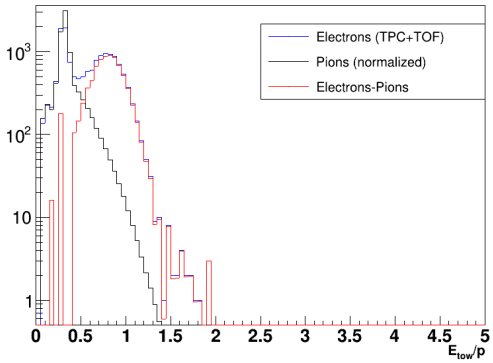

(a) $2.75 < p_T < 3.0$ GeV/c

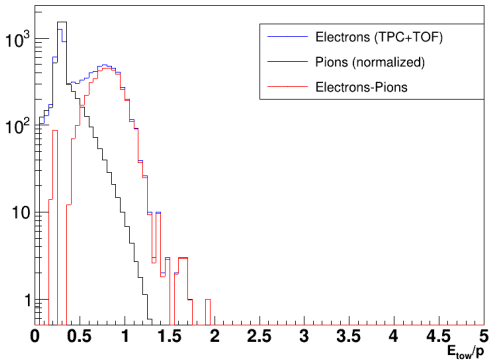

(b) $3.0 < p_T < 3.25$ GeV/c

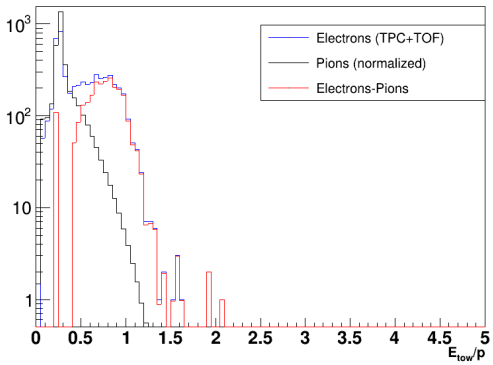

(c) $3.25 < p_T < 3.5$ GeV/c

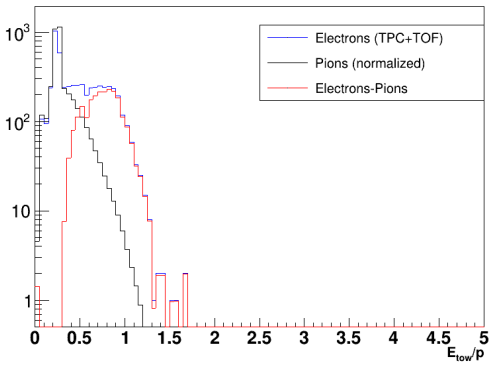

(d) $3.5 < p_T < 4.0$ GeV/c

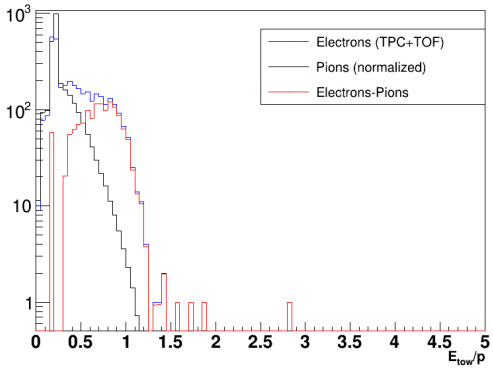

(e) $4.0 < p_T < 5.0$ GeV/c

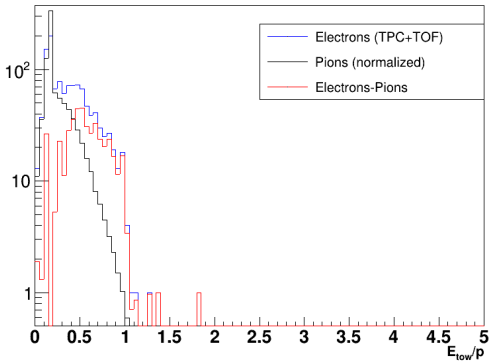

(f) $5.0 < p_T < 6.0$ GeV/c

Figure 4.5: E_{tow}/p vs p_T projections for electron tower energy, normalized pion tower energy and electrons-normalized pions tower energy.

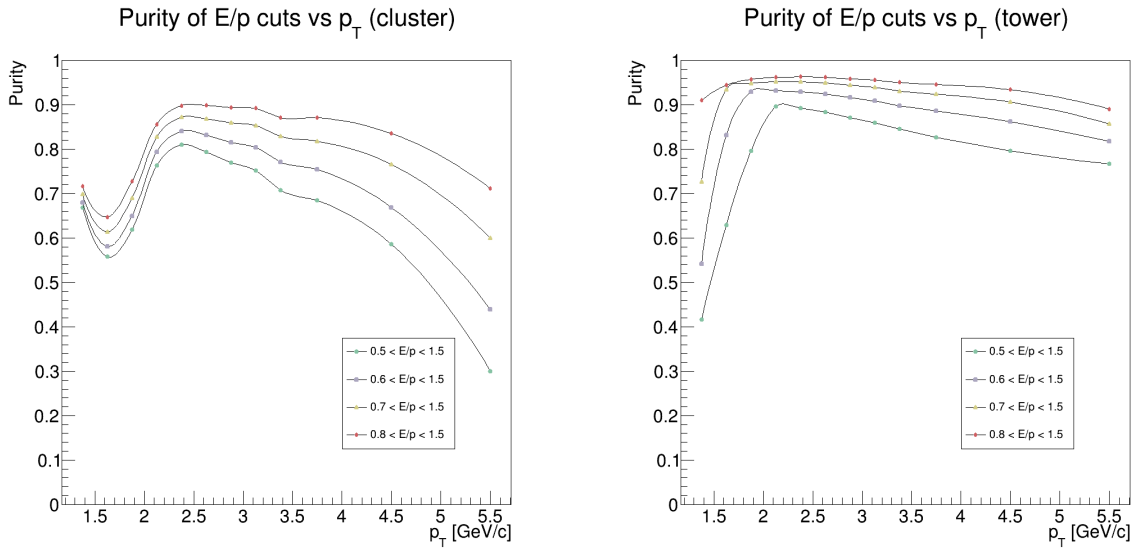

(a) Cluster energy (E_{cl}).

(b) Tower energy (E_{tow}).

Figure 4.6: Purity of E/p cuts vs p_T for cluster and tower energies. Pion normalization was performed using the integral of the peak region, i.e. $0.15 < p_T < 0.6$GeV/c.

4.3 Purity estimation - inclusive electrons

To estimate the purity of the inclusive electron sample, we base ourselves in the output of the TPC $n\sigma_{el}$ vs. p histogram after TOF and BEMC cuts have been applied. By doing a 1D projection histogram of $n\sigma_{el}$ in different p bins, we obtain multiple histograms corresponding to the electron distributions along with the hadron contamination sources.

The resulting projections are described as a sum of gaussians corresponding to different particles. In this analysis we consider the contamination from pions, merged pions, kaons and protons. Other possible contamination sources are not included here, since they lie far from electrons in $n\sigma$ values.

With the purpose of finding the parameters to the total fits in different p bins, we apply strict cuts in $n\sigma_K$, $n\sigma_p$, $n\sigma_{merged\pi}$, $n\sigma_{PE}$ distributions before the electron identification cuts are introduced (see Table 4.2). By extracting the mean and the sigma of the pure sample distributions of protons, kaons, merged pions and photonic electrons, we can provide constraints to the total multigaussian fit. The description of the sum becomes then more accurate, mainly in the region where overlapping of $n\sigma$ distributions happen.

Single particle distributions with the extracted parameters are displayed in Figures 4.7 - 4.10 for low, intermediate and high p. With the exception of the obtained yield, which becomes different after electron identification cuts are applied, the other parameters restrict the intervals for the fitting of the sum. Figure 4.11 display the fitting of the total $n\sigma$ distribution at low, intermediate and high p.

Cuts on $n\sigma_x$	
$n\sigma_P$	< 4
$n\sigma_\pi$	< 4
$n\sigma_{merged\pi}$	< 5
$n\sigma_{PE}$	< 2.5

Table 4.2: Strict $n\sigma$ cuts on single particle distributions.

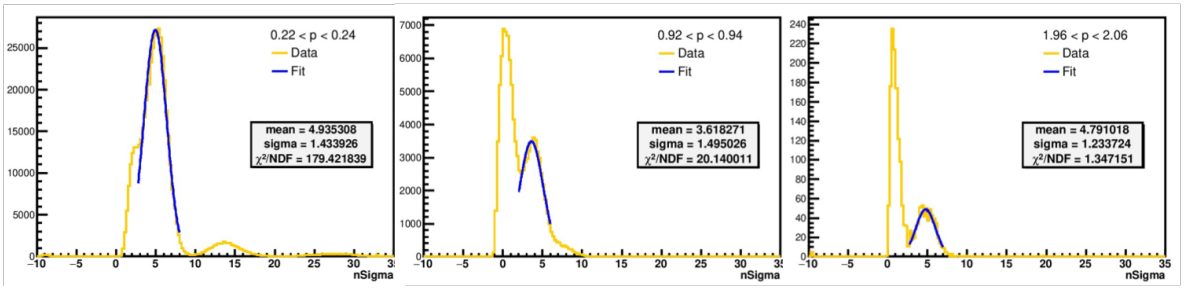

Figure 4.7: $n\sigma$ projections and fittings for merged pions before electron identification cuts at low, intermediate and high p.

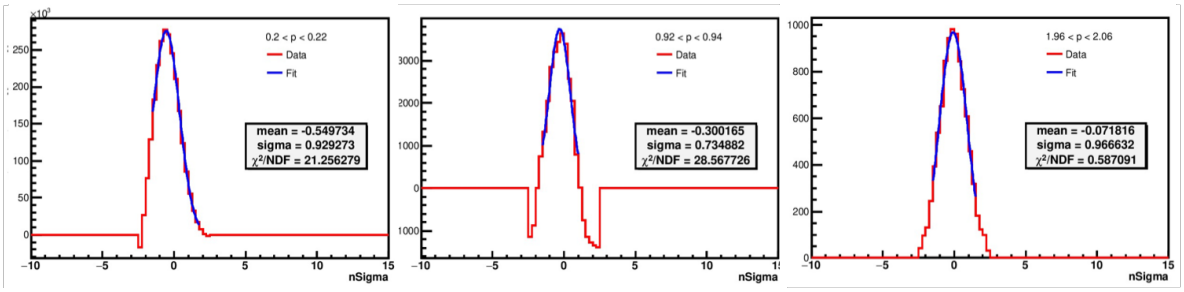

Figure 4.8: $n\sigma$ projections and fittings for photonic electrons before electron identification cuts at low, intermediate and high p.

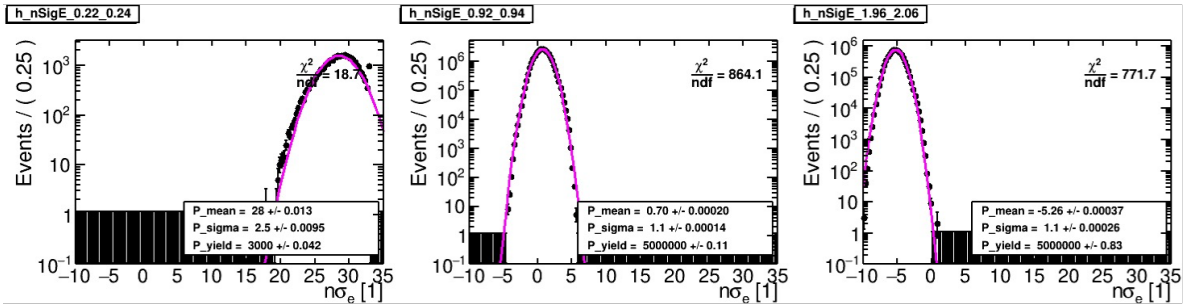

Figure 4.9: $n\sigma$ projections and fittings for protons before electron identification cuts at low, intermediate and high p.

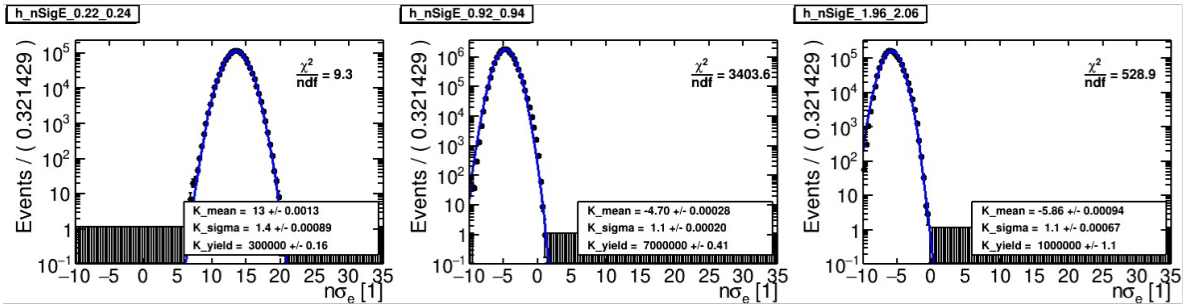

Figure 4.10: $n\sigma$ projections and fittings for kaons before electron identification cuts at low, intermediate and high p.

As Figure 4.11 shows, more work is needed to obtain the accurate purity from the $n\sigma$ distributions. From Figures 4.12a and 4.12b, it is also possible to notice that the large errors found for the $n\sigma_\pi$ parameters are probably the reason why the fits are still not working. This result is necessary to correct the inclusive electron yield, as given by Equation 3.1, and needs to be further analysed.

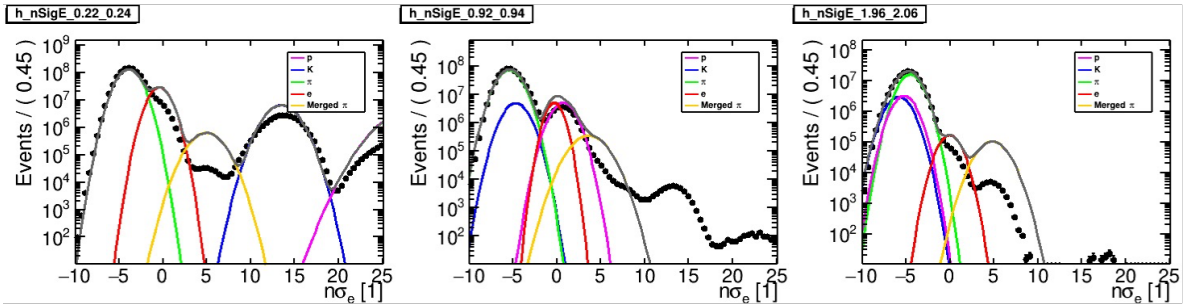

Figure 4.11: Totals $n\sigma$ projection and fittings at low, intermediate and high p.

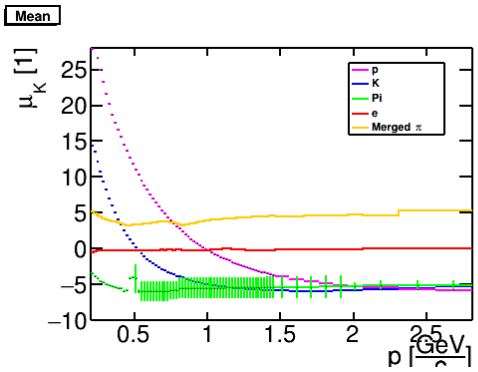

(a) Mean vs. p.

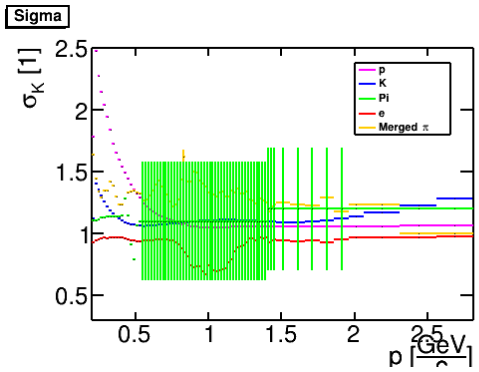

(b) Sigma vs p.

Figure 4.12: Mean and sigma according to momentum obtained in the multigaussian fit, using the constraints provided by the single particle distributions.

Chapter 5

Conclusions & Outlook

In summary, we have succesfully implemented the recently available BEMC information for this dataset to our analysis.

Starting with a QA of the BEMC towers, we were able to identify the hot towers that can affect the accuracy of our analysis. This information, when shared with the STAR Collaboration, can improve other studies using the same dataset.

When analysing the BEMC information, we estimated the purity of the E/p cuts to check which energy measurement to cut on for electron identification. In the case of our study, which uses data from heavy-ion collisions, the cut will be applied on the tower energy E_{tow}. From this result, cuts on the TPC $n\sigma_{el}$ and on TOF $1/\beta$ can be loosened in order to increase statistics, which is of major meaning to identify NPE electrons.

Moreover, we have concluded and initiated important steps in our NPE analysis. The invariant mass distribution of e^+e^- pairs was obtained, meaning that photonic electrons were already identified. After finishing the purity studies, we will be able to correct the yield of inclusive electrons. The next step consists mostly in performing the simulations of the detectors to correct the yield of photonic and non-photonic electrons. After these steps are accomplished, the calculation of the NPE yield along with their modification factors R_{AA} and/or R_{CP} becomes straightforward.

Bibliography

[1] Matic Lubej. *Standard Model Diagram.* URL: https://www.physik.uzh.ch/groups/serra/StandardModel.html.

[2] Manuel Lorenz. "Geladene Kaonen Produktion in Ar+KCl Reaktionen bei 1.756 AGeV". PhD thesis. Universität Frankfurt, 2008.

[3] Francesco Prino and Ralf Rapp. "Open heavy flavor in QCD matter and in nuclear collisions". In: *Journal of Physics G: Nuclear and Particle Physics* 43.9 (2016). ISSN: 13616471. DOI: 10.1088/0954-3899/43/9/093002.

[4] Xin Dong, Yen-Jie Lee, and Ralf Rapp. "Open Heavy-Flavor Production in Heavy-Ion Collisions". In: *Annual Review of Nuclear and Particle Science* 69 (Oct. 2019), pp. 417–445. DOI: 10.1146/ANNUREV-NUCL-101918-023806. URL: https://www.annualreviews.org/doi/abs/10.1146/annurev-nucl-101918-023806.

[5] ALICE Collaboration. "Direct observation of the dead-cone effect in QCD". In: (June 2021). URL: https://arxiv.org/abs/2106.05713v1.

[6] Barbara Betz. "Jet Propagation and Mach-Cone Formation in (3+1)-dimensional Ideal Hydrodynamics". In: (Oct. 2009). URL: https://arxiv.org/abs/0910.4114v1.

[7] T. Matsui and H. Satz. "J/ψ suppression by quark-gluon plasma formation". In: *Physics Letters B* 178.4 (1986), pp. 416–422. ISSN: 03702693. DOI: 10.1016/0370-2693(86)91404-8.

[8] A. Andronic et al. "Heavy-flavour and quarkonium production in the LHC era: from proton–proton to heavy-ion collisions". In: *European Physical Journal C* 76.3 (2016). ISSN: 14346052. DOI: 10.1140/epjc/s10052-015-3819-5.

[9] David Tlustý. "Open charm hadron production via hadronic decays at STAR". In: *Nuclear Physics A* 910-911 (2013), pp. 289–292. ISSN: 03759474. DOI: 10.1016/j.nuclphysa.2012.12.098.

[10] Helmut Satz. "Extreme States of Matter in Strong Interaction Physics". In: Lecture Notes in Physics 841 (2012). DOI: 10.1007/978-3-642-23908-3. URL: http://link.springer.com/10.1007/978-3-642-23908-3.

[11] B. I. Abelev et al. "Transverse momentum and centrality dependence of high-pT nonphotonic electron suppression in Au+Au collisions at sNN=200GeV". In: *Physical Review Letters* 98.19 (2007), pp. 1–6. ISSN: 00319007. DOI: 10.1103/PhysRevLett.98.192301.

[12] Wei Xie. "Heavy flavor results from STAR". In: *Nuclear Physics A* 904-905 (2013), pp. 170c–177c. ISSN: 03759474. DOI: 10.1016/j.nuclphysa.2013.01.059. URL: http://dx.doi.org/10.1016/j.nuclphysa.2013.01.059.

[13] Olga Rusňáková. "Measurements of non-photonic electrons with the STAR experiment". In: *Journal of Physics: Conference Series* 612.1 (2015). ISSN: 17426596. DOI: 10.1088/1742-6596/612/1/012034.

[14] Róbert Vértesi. "Heavy Flavor Measurements at STAR". In: *Nuclear and Particle Physics Proceedings* 273-275 (2016), pp. 1588–1594. ISSN: 24056014. DOI: 10.1016/j.nuclphysbps.2015.09.257.

[15] Xiaozhi Bai. "Measurements of Open Heavy Flavor Production in Semi-leptonic Channels at STAR". In: *Nuclear Physics A* 956 (2016), pp. 513–516. ISSN: 03759474. DOI: 10.1016/j.nuclphysa.2016.03.027. URL: http://dx.doi.org/10.1016/j.nuclphysa.2016.03.027.

[16] J. Adam et al. "Measurement of the production of high-pT electrons from heavy-flavour hadron decays in Pb–Pb collisions at sNN=2.76 TeV". In: *Physics Letters, Section B: Nuclear, Elementary Particle and High-Energy Physics* 771 (2017), pp. 467–481. ISSN: 03702693. DOI: 10.1016/j.physletb.2017.05.060.

[17] S. Acharya et al. "Measurement of electrons from semileptonic heavy-flavour hadron decays at midrapidity in pp and Pb–Pb collisions at sNN=5.02 TeV". In: *Physics Letters, Section B: Nuclear, Elementary Particle and High-Energy Physics* 804 (2020), pp. 1–15. ISSN: 03702693. DOI: 10.1016/j.physletb.2020.135377.

[18] Xu Sun. "Flow in the RHIC beam energy scan from STAR". In: *Journal of Physics: Conference Series* 535.1 (2014). ISSN: 17426596. DOI: 10.1088/1742-6596/535/1/012005.

[19] Bedangadas Mohanty. "STAR experiment results from the beam energy scan program at the RHIC". In: *Journal of Physics G: Nuclear and Particle Physics* 38.12 (2011). ISSN: 09543899. DOI: 10.1088/0954-3899/38/12/124023.

[20] Lokesh Kumar. "Review of recent results from the RHIC beam energy scan". In: *Modern Physics Letters A* 28.36 (2013). ISSN: 02177323. DOI: 10.1142/S0217732313300334.

[21] Lokesh Kumar. "STAR Results from the RHIC Beam Energy Scan-I". In: *Nuclear Physics A* 904-905 (2013), pp. 256c–263c. ISSN: 03759474. DOI: 10.1016/j.nuclphysa.2013.01.070.

[22] Yi Yang. "The STAR detector upgrades for the BES II and beyond physics program". In: *Nuclear Physics A* 1005.November (2021). ISSN: 03759474. DOI: 10.1016/j.nuclphysa.2020.121758.

[23] W. J. Llope et al. "The STAR vertex position detector". In: *Nuclear Instruments and Methods in Physics Research, Section A: Accelerators, Spectrometers, Detectors and Associated Equipment* 759 (2014), pp. 23–28. ISSN: 01689002. DOI: 10.1016/j.nima.2014.04.080. URL: http://dx.doi.org/10.1016/j.nima.2014.04.080.

[24] M. Anderson et al. "The STAR time projection chamber: A unique tool for studying high multiplicity events at RHIC". In: *Nuclear Instruments and Methods in Physics Research, Section A: Accelerators, Spectrometers, Detectors and Associated Equipment* 499.2-3 (2003), pp. 659–678. ISSN: 01689002. DOI: 10.1016/S0168-9002(02)01964-2.

[25] Dong Xin. "The time-of-flight detector for RHIC/STAR and the related physics". In: *AIP Conference Proceedings* 865.2006 (2006), pp. 332–337. ISSN: 0094243X. DOI: 10.1063/1.2398870.

[26] M. Beddo et al. "The STAR barrel electromagnetic calorimeter". In: *Nuclear Instruments and Methods in Physics Research, Section A: Accelerators, Spectrometers, Detectors and Associated Equipment* 499.2-3 (2003), pp. 725–739. ISSN: 01689002. DOI: 10.1016/S0168-9002(02)01970-8.

[27] David Hofman. "Measurements of Upsilon Production in p + p , p + Au and Au + Au Collisions at 200 GeV with the STAR Experiment". PhD thesis. University of Illinois at Chicago, 2019.

[28] P. A. Zyla et al. "Review of particle physics". In: *Progress of Theoretical and Experimental Physics* 2020.8 (2020), pp. 1–2093. ISSN: 20503911. DOI: 10.1093/ptep/ptaa104.